# Assessing the role of clay and salts on the origin of MARSIS basal bright reflections

Elisabetta Mattei[1], Elena Pettinelli[1*], Sebastian Emanuel Lauro[1], David E. Stillman[2], Barbara Cosciotti[1], Lucia Marinangeli[3], Anna Chiara Tangari[3], Francesco Soldovieri[4], Roberto Orosei[5] and Graziella Caprarelli[6]

Corresponding author: elena.pettinelli@uniroma3.it

Affiliations:

[1] Dipartimento di Matematica e Fisica, Università degli studi Roma Tre, Rome, Italy

[2] Department of Space Studies, Southwest Research Institute, Boulder, USA

[3] Dipartimento di Scienze Psicologiche, della Salute e del Territorio, Università degli studi "G. D'Annunzio" Chieti – Pescara, Chieti, Italy

[4] Istituto per il Rilevamento Elettromagnetico dell'Ambiente, Consiglio Nazionale delle Ricerche, Naples, Italy

[5] Istituto di Radioastronomia (IRA), Istituto Nazionale di Astrofisica (INAF), Bologna, Italy

[6] Centre for Astrophysics, Institute for Advanced Engineering and Space Sciences, University of Southern Queensland, Toowomba, Australia

**Highlights**

- Bright basal reflections have been detected by MARSIS at Ultimi Scopuli, Mars
- High permittivity contrast between the ice and the basal material is required
- Wet sediments or ponded water have been suggested as the cause of such reflections
- Hydrous minerals and salts are considered as possible alternative to basal water
- Only brines can generate such high dielectric contrast at low basal temperature

34

**Abstract**

Anomalously bright basal reflections detected by MARSIS at Ultimi Scopuli have been interpreted to indicate the presence of water-saturated materials or ponded liquid water at the base of the South Polar Layered Deposits (SPLD). Because conventional models assume basal temperatures ($\leq$200K) much lower than the melting point of water, this interpretation has been questioned and other explanations for the source of the bright basal reflections have been proposed, involving clay, hydrated salts, and saline ices. Combining previous published data, simulations, and new laboratory measurements, we demonstrate that the dielectric properties of these materials do not generate strong basal reflections at MARSIS frequencies and Martian temperatures. Plausible candidates remain perchlorates and chlorides brines that exhibit a strong dielectric response at much lower temperatures than other materials. This explanation might require that metastability could be maintained for a long period of time on a geological scale.

## 1. Introduction

In the last fifty years, terrestrial Radar Echo Sounding (RES) technique has played a fundamental role in detecting subglacial liquid water and understanding the hydrological processes beneath Antarctica and Greenland ice sheets (Siegert, 2018). Planetary radar sounders could now play a similar role for Mars. Recently, MARSIS (Mars Advanced Radar for Subsurface and Ionosphere Sounding), onboard Mars Express spacecraft, detected bright reflections from the base of the Martian South Polar Layered Deposits (SPLD) at Ultimi Scopuli (Orosei et al., 2018; Lauro et al., 2021). Such reflections have characteristics comparable to those acquired by terrestrial RES above subglacial water ponded areas (Lauro et al., 2021), and were therefore interpreted as caused by (partially) water-saturated materials and/or layers of liquid water. Given the low temperatures commonly inferred at the base of the SPLD (of the order of 200 K or lower) (Wieczorek, 2008; Plesa et al., 2018; Sori and Bramson, 2019), liquid water can only exist as a aqueous solutions of salts known to strongly depress the freezing point of water, such as perchlorates, chlorates and chlorides [e.g., Chevrier et al. (2009); Toner, and Catling (2018); Primm et al. (2020); Stillman et al. (2021)]. Briny waters are common in terrestrial glacial environments and are considered to be

some of the brightest englacial or subglacial reflectors detectable with radar sounders [e.g., Nobes et al. (2005); Grima et al. (2016); Rutishauser et al. (2018)].

Other subglacial water-saturated sediments, especially clay, could however also produce a strong radar response [e.g., Tulaczyk and Foley (2020)]. On Mars, clay and other hydrous mineral bearing deposits have been identified in many outcrops both remotely by OMEGA (Observatoire pour la Minéralogie, l'Eau, les Glaces, et l'Activité) (Bibring et al., 2006) onboard Mars Express and CRISM (Compact Reconnaissance Imaging Spectrometer for Mars) onboard Mars Reconnaissance Orbiter (Murchie et al., 2007), and in situ by the NASA Spirit and Curiosity rovers at the Gusev and Gale craters landing sites [e.g., Clark et al. (2007); Bristow et al. (2018); Rampe et al. (2020a)]. Though no clear evidence of clay and salt outcrops in the terrains surrounding the SPLD has been reported so far, their presence in the sediments at the base of the ice cannot be positively ruled out. To assess the possibility that clay-rich sediments could produce basal reflections as strong as those detected by MARSIS [e.g., Bierson et al. (2021); Smith et al. (2021)], we performed dielectric laboratory measurements on Martian clay analogs. Here we compare our results to previously published work on the dielectric properties of clay and salts at Martian temperatures, and to data obtained from MARSIS observations at Ultimi Scopuli. We also discuss the role of specific briny materials in the generation of bright basal reflections.

## 2.   Salts and clays on Mars

Hydrous minerals and salts are largely present on Mars: they have been found in samples of Martian meteorites (Gooding and Muenow, 1986; Treiman et al., 1993; McSween, 1994; Leshin and Vicenzi, 2006; Muttik et al., 2014; Kounaves et al., 2014), and detected through orbital and lander observations (Murchie et al., 2009; Ehlmann and Edwards, 2014). The formation of hydrous minerals has been explained by a variety of processes, including late volcanic/hydrothermal activity, low-grade metamorphism, deposition by migrating groundwaters, surface deposition in fluvio-lacustrine or playa environments, adsorption of atmospheric water. Significant amounts of hydrous minerals have not been detected at high latitudes, where they are probably masked by a thin latitude dependent sedimentary layer (Mustard et al., 2001), and by polar processes. About 70% of phyllosilicates detections on Mars are of Fe/Mg smectites (nontronite, saponite) and chlorite, followed in abundance by Al-smectites (montmorillonite, beidellite) (Ehlmann et al., 2011). Quantitative analysis based on Curiosity rover measurements indicate an amount of clay minerals ranging between 3 and 28% in fluvio-lacustrine sediments of Gale Crater mainly containing smectite (Bristow et al., 2018; Rampe et al., 2020a). VNIR spectral analysis by orbiter

suggest abundances of 20–65 % clay (Fe-Mg clays) in Mawrth Vallis, representing the highest values measured on Mars (Poulet et al., 2008). Thermal infrared spectra (TIR), indicate a clay abundance of about 15 % in the southern highlands, while the amounts of clays do not exceed 30% in Nili Fossae, Tyrrhena Terra, and Terra Sirenum (Poulet et al., 2008; Ehlmann et al., 2013). Clays and salts may host significant amount of water. Recent estimates of the water content in Gale crater sedimentary sequence show an interquartile range of 2.3–3.1 wt.% $H_2O$ likely associated to adsorbed water, molecular water of hydrated minerals, salts and amorphous phases (Thomas et al., 2020).

Based on the stratigraphic distribution of clay and other minerals association, clay deposits on Mars can be associated to three geological environments (Ehlmann et al., 2011; Ehlmann et al., 2013) (Fig.1):

i) *crustal clays*, which include Mg-rich smectite (saponite) and chlorite minerals originated from hydrothermal alteration, metamorphism and burial diagenesis (as demonstrated by laboratory experiment (Gaudin et al., 2018; Bishop et al., 2018; Tangari et al., 2020);

ii) *stratigraphic clays*, consisting of Fe/Mg smectite overlain by Al- bearing phyllosilicates (as kaolinite, montmorillonite and beidellite), late Noachian to Hesperian in age, often associated with sulphates.

iii) *sedimentary clays*, characterized by Fe/Mg smectite often in association with salts and carbonates, found in fluvial and paleolacustrine basins, such as Jezero and Gale Crater (Rampe et al., 2020a; Ehlmann et al., 2009).

Owing to the global surface distribution of hydrous minerals and salts, and their susceptibility to fragmentation and pulverization facilitating their spreading across the planet as part of the Martian dust (Ehlmann and Edwards, 2014), grains of salts and hydrous minerals are likely to be present as impurities in the water ice forming the polar caps, and as enriched components of the top layer of regolith at the base of the polar layered deposits.

Clays type
-  crustal
- stratigraphic
- sedimentary

| MAIN MINERALOGY based on Ehlmann et al., 2011-2013 | Fe/Mg smectite - chlorite - Al-clays (kaolinite, montmorillonite)- illite | Fe/Mg smectite - chlorite - Al-clays (kaolinite, montmorillonite, other unspecified) - silica - carbonates | Fe/Mg smectite - sulfate - Al-clays (other unspecified) |
|---|---|---|---|
| MARS sites | Argyre, Terra Sirenum, Nili Fossae | Valles Marineris, Arabia Terra | Jezero, Gale, Holden |
| EARTH analogues | Ch1, Ch2 | Sm2, Sm3, Sm4 | Sm1 |
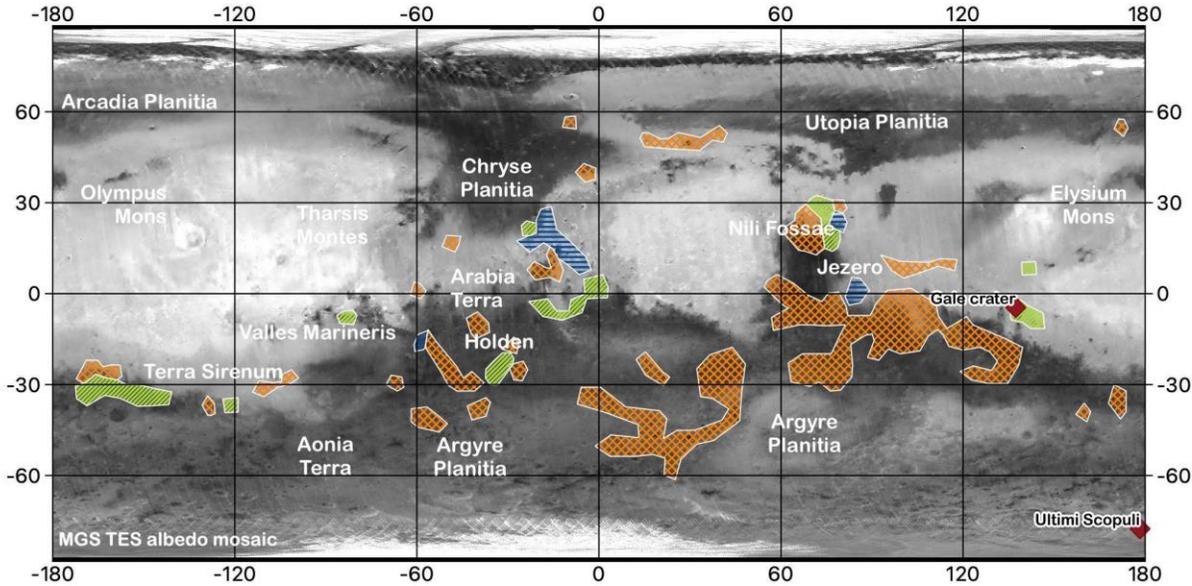


**Fig.1.** Distribution of clays on Mars. Crustal clays mostly contain Fe-Mg smectite and chlorite as evidence of bedrock alteration. Stratigraphic clays show association of Fe-Mg-Al-rich smectites with carbonates as result of deposition during the wettest period of Mars. Sedimentary clay is often associated with sulfates and chlorides. Potential correlation with used terrestrial analog samples is based on similarities with clay types (ref. to Table S1). Extent and type of clays mapped are from data in Ehlmann et al. (2011) and Ehlmann et al. (2013).

### 3. An overview on clay and salts dielectric properties

Clay sediments are composite materials: on Earth they are usually made of mineral grains, free water, air, clay aggregates (or clay platelets) and organic matter (Fig.2). Each component of the sediment has a specific dielectric response to an oscillating electric field (e.g., a radar wave) which is described by the complex (relative) dielectric permittivity:

$$\varepsilon = \varepsilon' + i\varepsilon'' \quad (1)$$

The real part of the dielectric permittivity ($\varepsilon'$) accounts for the polarizability of the material (energy storage) and the imaginary part ($\varepsilon''$) for the energy loss due to heat caused by the polarization process ($\varepsilon''_p$) and free charge carrier migration (conduction), as follows:

$$\varepsilon'' = \varepsilon''_p + \frac{\sigma_{DC}}{2\pi f \varepsilon_0} \quad (2)$$

145

where $\varepsilon_0 = 8.85 \cdot 10^{-12} F/m$ is the dielectric permittivity of a vacuum, $\sigma_{dc}$ is direct-current

conductivity and $f$ is the frequency. The quantities $\varepsilon'$ and $\varepsilon''$ depend on the frequency of the

applied electric field, the temperature of the material (T), water content and salinity (Olhoeft, 1981).

Apart from air (or free space) where $\varepsilon' = 1$, the only exception is given by the mineral grains

(including dry clay grains) for which $\varepsilon'$ only depends on density $\rho$ and $\varepsilon''$ is usually negligible

(Olhoeft, 1981; Liu and Mitchell, 2009).



152
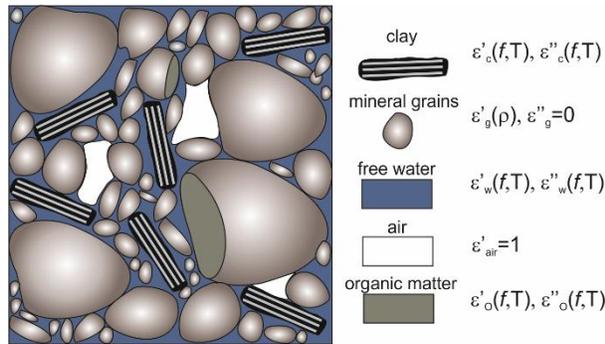
**Fig. 2.** Sketch of terrestrial unsaturated clay sediment dielectric properties. The overall complex dielectric permittivity
of a sediment is controlled by the volume fraction of the components and their specific dielectric response. Clay
particles are described here by a single value of the real and imaginary parts; however, such values are a combination
of various dielectric responses due to different forms of water inside the clay aggregates. Organic matter, typically
present in surface sediments on Earth, is absent or rare on Mars.

158

At a given temperature and for a relative volumetric fraction of each component, the clay sediment

dielectric spectra ($\varepsilon'(f)$ and $\varepsilon''(f)$) are a complex combination of the different dielectric

responses (Olhoeft, 1977; Lorek and Wagner, 2013). At terrestrial temperatures, the overall (bulk)

complex permittivity is generally dominated by free (salty) water (Fig. 2) as its real and imaginary

parts can be one-three orders of magnitude larger than those of the other components [e.g., Chelidze

et al. (1999), Ishida (2002)]. The dielectric effect of free water is removed if the clay sediment is

oven-dried or desiccated [e.g., Kuligiewicz and Derkowski (2017)]. However, such procedure does

not eliminate bound water, which may still have a high complex permittivity depending on

temperature and frequency (Liu and Mitchell, 2009) and thus could become dielectrically dominant,

especially for clays, such as smectite and vermiculite, that accommodate a large amount of

interlayer water (Lorek and Wagner, 2013; Johnston, 2010). On the other hand, if a wet clay

sediment is cooled below 273 K, free water confined in the pore space of the sediment and in the

clay aggregates starts to freeze, and its contribution to the overall complex permittivity becomes

172 progressively comparable to that of the mineral grains at MARSIS frequencies. Depending on

173 frequency, the dielectric behavior of bound water could become predominant, controlling the

174 overall complex dielectric permittivity of the material [e.g., Olhoeft (1977)].

175 As hydrated salts are often associated with clay minerals in the sediments, we first discuss their

176 contribution to the overall dielectric behavior of clay-rich sediments. Dielectric properties of

177 hydrated salts have been studied for almost a century [e.g., Burton and Turnbull (1937), Cheng

178 (1940), Kamiyoshi and Miyamoto (1950), Young and Frederikse (1973)]. It is well known that low

179 loss characterizes pure salt at frequencies between 1 MHz and 1 GHz, which results in large radar

180 signal penetration (Stewart and Unterberger, 1976). Dielectric measurements on different types of

181 hydrated salts in the MHz range at low and high temperatures (ref. to Table 1) indicate that the real

182 part of permittivity is mainly constant with temperature, and ranges between 4 and 8 (Parkhomenko,

183 1967), depending on the hydrated state of the crystal (Pettinelli et al., 2016). The imaginary part is

184 usually very low [e.g., Stewart and Unterberger, Parkhomenko (1967)]: the hydrated magnesian

185 sulfate meridianiite for example, has an almost constant value of the real part of permittivity in the

186 temperature interval 200-300 K, and a negligible imaginary part (Pettinelli et al., 2016). The real

187 part of jarosite is very low, and it is frequency and temperature independent within the range of

188 temperature 180-296 K and at frequencies between 1 MHz and 1 GHz (Stillman and Olhoeft, 2008).

189 Additionally, the loss term is below the measurement limit of the instrument, which indicates its

190 direct-current conductivity is less than $6.67 \times 10^{-5}$ S/m.

191

192 **Table 1 Real and imaginary parts of permittivity of some hydrous minerals of interest for Mars.**

193

| Hydrated salts | | | | | | |
|---|---|---|---|---|---|---|
| | ε' | ε'' | Frequency | Temperature | Reference | Sample |
| Meridianiite | 4.7 | ~0 | 1MHz | 200K | Pettinelli et al. (2016) | Solid |
| Jarosite | 3.07 | ~0 | 1MHz | 180-296K | Stillman and Olhoeft, 2008 | Granular |
| | | | | | | |
| Gypsum | 6.4 | 0.01 | 1 MHz | 298K | Olhoeft (1979) | Solid |
| Anhydrite | 6.9 | 0.06 | 1 MHz | 298K | Olhoeft (1979) | Solid |
| | | | | | | |
| Dry clay | | | | | | |
| Chlorite | 7.4 | 1.5 | 1 MHz | 298K | Olhoeft (1979) | Solid |
| Kaolinite | 4.6 | ~0 | 30MHz | 298K | Saarenketo (1998) | Solid |
| Nontronite | 3.7 | 0.08 | 10MHz | 220K | Cunje et al. (2018) | Granular |
| Ca-montmorillonite (STx-1b) | 3.6 | 0.08 | 10MHz | 220K | Cunje et al. (2018) | Granular |
| Ca-bentonite | 3.5 | 0.07 | 1MHz | 298K | Saltas et al. (2008) | Granular |

200

201 The dielectric response of clay minerals is particularly complex [e.g., Liu and Mitchell (2009),

202 Sposito and Prost (1982), Cadène et al. (2006)] due to their retention properties. As smectite is the

203 most common type of clay mineral detected on Mars, we focus here mainly on the properties of this

204 group, though all clays share a common dielectric behavior. Smectites have an expanding lattice,

205 with their layers easily separated by water, and are characterized by a large cation exchange

206 capacity. The number of water molecules that can be accommodated between layers depends on
207 the interlayer cation species and the relative humidity (Johnston, 2010). In general, clay aggregates
208 contain three forms of water: interlayer water, electrostatic double layer water, and free porewater
209 (Wersin et al., 2004). The interlayer water is bound to the exchangeable cations (counterions) and/or
210 to the negatively charged clay particle surfaces, whereas the electrostatic double layer forms a
211 transition zone between the mineral grain surface and the free water confined in the interparticle or
212 interaggregate space. These forms of water have different dielectric response (i.e., different $\varepsilon'$ and
213 $\varepsilon''$) depending on the frequency of the applied electric field and the temperature of the material,
214 which combine in a complicated manner. The dielectric properties of smectites have been
215 extensively studied by several authors at different temperature, frequencies, and water content
216 conditions [e.g., Liu and Mitchell (2009), Sposito and Prost (1982), Cadène et al. (2006), Kaviratna
217 et al. (1996), Kaden et al. (2013)]. In the MHz range, the real part of permittivity of solid clay grains
218 varies between 4 and 8, and remains nearly constant with temperature [e.g., Olhoeft (1979),
219 Saarenketo (1998)] (see Table 1). At low temperature (220 K) dry smectites (montmorillonite and
220 nontronite) exhibit very low values of complex permittivity that do not appreciably change with
221 frequency (Cunje et al., 2018; Kułacz et al., 2021). However, at 298 K and 1 MHz, wet smectite
222 sediments have fairly different dielectric behavior, with real and imaginary parts of permittivity
223 reaching values of the order of $10^2$ and $10^3$, respectively (Kaden et al., 2013; Kułacz and
224 Orzechowski, 2019). Conversely, extensive literature data indicate that at low temperature (well
225 below 273 K) the complex dielectric permittivity of wet clay sediments (montmorillonite, bentonite
226 or nontronite enriched) drops significantly, sometimes reaching values close to those of dry clays
227 [e.g., Lorek and Wagner (2013), Cunje et al. (2018), Kułacz and Orzechowski (2019), Moore and
228 Maeno (1993), Bittelli et al. (2004), Stillman et al. (2010)].

229

230 **4. Radar reflection and apparent permittivity**

231 MARSIS retrieved permittivity values are estimated from the amplitude of the reflected signal. The
232 reflection coefficient $\Gamma_{12}$ of a normally impinging plane wave at an interface between two adjacent
233 materials depends on the complex dielectric permittivity of such materials (i.e., their dielectric
234 contrast) as follows:

235

$$236 \quad \Gamma_{12} = \frac{\sqrt{\varepsilon'_1 + i\varepsilon''_1 + i\dfrac{\sigma_{1_{DC}}}{2\pi f \varepsilon_0}} - \sqrt{\varepsilon'_2 + i\varepsilon''_2 + i\dfrac{\sigma_{2_{DC}}}{2\pi f \varepsilon_0}}}{\sqrt{\varepsilon'_1 + i\varepsilon''_1 + i\dfrac{\sigma_{1_{DC}}}{2\pi f \varepsilon_0}} + \sqrt{\varepsilon'_2 + i\varepsilon''_2 + i\dfrac{\sigma_{2_{DC}}}{2\pi f \varepsilon_0}}} \quad (3)$$

237

238 Equation (3) shows that $\Gamma_{12}$ is, in general, a complex quantity, which would require information on

239 the modulus and phase of the reflected signal to be solved. Conversely, MARSIS data lack the

240 information on the signal polarity and only allow to estimate $|\Gamma_{12}|$, which is a real quantity.

241 Therefore, MARSIS does not allow to separately compute real and imaginary parts of the complex

242 permittivity. Nevertheless, if some assumption on the permittivity of the first layer can be made,

243 for example that the loss term is negligible ($\varepsilon_1 = \varepsilon_1'$), it is still possible to estimate the dielectric

244 properties of the second layer introducing the concept of the apparent permittivity $\varepsilon_a$:

245

$$246 \quad |\Gamma_{12}| = \frac{\sqrt{\varepsilon_a} - \sqrt{\varepsilon_1}}{\sqrt{\varepsilon_a} + \sqrt{\varepsilon_1}} \quad (4)$$

247

248 under the assumption that the permittivity of the second layer is larger than that of the first layer.

249 Note that Eqn.4 can be slightly modified if the permittivity of the second layer is lower. The quantity

250 $\varepsilon_a$ is analytically obtained as (see Appendix A):

251

$$252 \quad \varepsilon_a = \varepsilon_1 \left[ \frac{1 + |\Gamma_{12}|}{1 - |\Gamma_{12}|} \right]^2 = \varepsilon_1 \frac{\varepsilon_1 + |\varepsilon_2| + \sqrt{\varepsilon_1^2 + |\varepsilon_2|^2 - 2\varepsilon_1\varepsilon_2'}}{\varepsilon_1 + |\varepsilon_2| - \sqrt{\varepsilon_1^2 + |\varepsilon_2|^2 - 2\varepsilon_1\varepsilon_2'}} \quad (5)$$

253

254 It is important to point out that the apparent permittivity is a real quantity that accounts for both

255 polarization and conductive processes and fully describes the dielectric properties of a material.

256 Such quantity should not be confused with the real part of permittivity $\varepsilon_2'$, as it accounts for both

257 real and imaginary parts of the basal permittivity $\varepsilon_2$ and represents the value that MARSIS would

258 detect if such material lay below the SPLD. We use equation (5) to compute the apparent

259 permittivity using real and imaginary parts of published data and laboratory measurements on clay

260 sediments and salt solutions, assuming for the SPLD a permittivity value $\varepsilon_1' = 3.5$. Values

261 computed with Equation (5) were compared to those retrieved from MARSIS data inversion in the

262 bright reflection area at Ultimi Scopuli (Orosei et al., 2018; Lauro et al., 2021). Specifically, we

263  will use the median value ($\varepsilon_a = 33$) as the threshold against which to compare and discuss the

264  results in this work.  Such median refers to the statistical distribution of the apparent permittivities

265  retrieved by MARSIS at 4 MHz at the base of the SPLD at Ultimi Scopuli (Orosei et al., 2018).

266  Such distribution indicates that there is a probability of 75% to obtain an apparent permittivity value

267  $\varepsilon_a \geq 16$.

268

## 5. Analysis of previous studies of dielectric properties of clays at Martian temperatures

270  We selected published data that allow the estimation of the apparent permittivity at 1 MHz (the

271  closest to MARSIS frequencies common to all available data) for a set of smectites samples having

272  different clay percentage, water content and salt solution concentration (Table 2).

273

274  **Table 2. Properties and measurement conditions of clay samples used to compute the apparent permittivity at**

275  **1MHz from reference data.**

| Clay type | Clay content | Water content | Salt solution | Temperature range | Frequency range | Reference |
|---|---|---|---|---|---|---|
| Smectite (Ca-Montmorillonite) | 9.67 vol % of STx-1* | 0.22-1.34 wt% | 1 M CaCl2 | 183K - 298K | 1 mHz - 1 MHz | Stillman and Grimm (2011a) |
| Ca-Bentonite | 65-70% wt% | 9.27 wt% | - | 203K – 293K | 10Hz - 1.1 MHz | Lorek and Wagner (2013) |
| Natural nontronite | (~95 wt%) | 21wt% | - | 173K – 373K | 25 Hz–1 MHz | Kułacz and Orzechowski (2019) |
| Ca-Montmorillonite(1) | (20 v% SAz**) | 80 v% | 0.1 M CaCl2 | 180-298 K | 1 mHz - 1 MHz | Stillman et al. (2010) |
| Ca-Montmorillonite(2) | (20 v% SAz**) | 80 v% | 0.001 M CaCl2 | 180-298 K | 1 mHz - 1 MHz | Stillman et al. (2010) |
| Ca-Montmorillonite(3) | (46 v% SAz**) | 10 v%/44% air | deionized water | 180-298 K | 1 mHz - 1 MHz | Stillman et al. (2010) |

276  *(≥95% montmorillonite)

277  **(≥95% montmorillonite)

278

279  Among those, we selected two temperatures: 203K, the lowest value common to all measurements

280  reported in Table 2 and 230K a temperature slightly higher than the mean surface temperature on

281  Mars (~220K in Stillman and Grimm (2011a)). The apparent permittivity of the dataset computed

282  at 1 MHz highlights the large variability (from 2.6 to 31.8) of the clay dielectric response (Fig. 3).

283  Smectite and Ca-bentonite samples exhibit the lowest values (2.6-4.7) (Table 2) probably because

284  of low water content, that do not appreciably change with temperature.  The apparent permittivity

285  of the Ca-montmorillonite and nontronite samples at 203 K does not exceed 13; however, at 230 K

286  the apparent permittivity of the Ca-montmorillonite increases up to 20.1 for sample 1 and 16.0 for

287  sample 2, respectively. Such increase is probably due to the liquid brines in the samples, as they

288  were prepared by mixing the clay with a large amount of $CaCl_2$ solutions (Table 2), which has an

289  eutectic temperature < 230 K (Grimm et al., 2008).  The highest value is reached by the almost pure

290  sample (95%) of natural nontronite with 21% of water content (Kułacz and Orzechowski, 2019).

291  These data suggest that for a temperature at the base of the SPLD > 230 K, some of the analyzed

clay samples could potentially produce relatively strong reflections. However, according to both theoretical and experimental evidence, the apparent permittivity of clay sediments should decrease at higher frequencies [e.g., Lorek and Wagner (2014), Kułacz and Orzechowski (2019), Stillman and Grimm (2011b), Kao (2004)]. Therefore, values at 1 MHz should be considered an overestimation relative to those measured at 4 MHz and must therefore be corrected before being compared with MARSIS data.
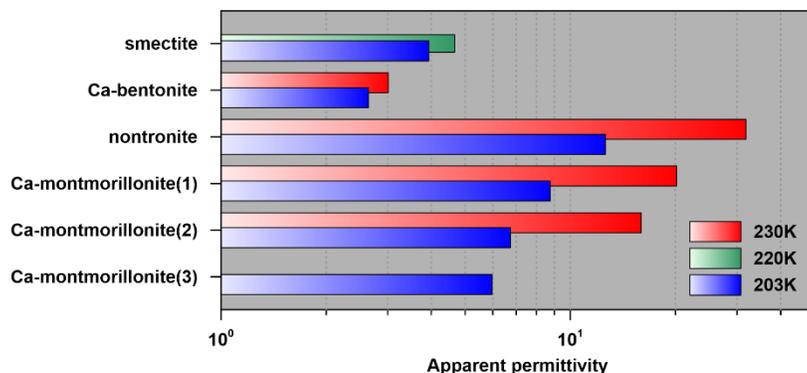


**Fig. 3** Apparent permittivity at 1 MHz from literature data. Values of the apparent permittivity computed at 203 K and 230 K (220 K is from Stillman and Grimm (2011a), ref. to Table 2) from real and imaginary parts measured at 1 MHz on various smectite samples. The samples have different water content, clay content and salt solutions (Table 2).

Because the nontronite sample exhibits the highest apparent permittivity and is a common mineral in the Martian clay sediments, we used Kułacz and Orzechowski's (2019) experimental dataset to compute its apparent permittivity at 4 MHz, by shifting low temperature data to higher frequencies (according to the method proposed by Stillman and Grimm (2011a). After correction, we found that the apparent permittivity at 203 K did not appreciably change from that at 1 MHz (~13), whereas at 230 K the value at 4 MHz decreases to 25.1. Moreover, as the nontronite sample is almost pure and the clay content detected in Martian terrains is highly variable (ranging between 3 and 65 wt%) we used the Complex Refractive Index Model (CRIM) (Sihvola, 1999) to evaluate the effect of the nontronite content (expressed in volume fraction) on the overall apparent permittivity of a clay sediment (Fig. 4). We assumed the composition of the sediments to be: i) basaltic grains, air and nontronite (desiccated Martian model) (Fig. 4A); ii) basaltic grains, water ice and nontronite (water ice saturated Martian model) (Fig. 4B); and iii) basaltic grains, liquid water and nontronite (terrestrial analog) (Fig. 4C). Mixing models were computed at 203 K, 230 K and 287 K for a volume fraction of nontronite ranging from 0 to 1. Permittivity values for the basalt grains and water ice are those published by Mattei et al. (2014), liquid water values are from Kaatze (1989), and those for natural nontronite (21 wt% $H_2O$) are by Kułacz and Orzechowski (2019). As expected,

319    the apparent permittivity values computed at 230 K are higher than those at 203 K and the values

320    computed for the model with water ice in the pores are slightly larger than those with air-filled

321    pores (Fig. 4D). The nontronite content produces a clear increase in the overall apparent

322    permittivity: for example, 50% of nontronite content increases the apparent permittivity from 5.2

323    (0%) to 13.1 in the simulation with ice. Even so, both plots at 203 K and 230 K are below MARSIS

324    threshold value ($\varepsilon_a = 33$), converging toward the values of (almost) pure nontronite at 4 MHz (25.1

325    at 230 K and 12.6 at 203 K). Conversely, in the terrestrial water-saturated clay sediment simulation

326    (287 K) MARSIS retrieved value is reached with 14% of nontronite content, whereas for dry

327    sediment, we need at least 35% of nontronite volume fraction. The pink shaded area in Fig.4D

328    delimits the region where the apparent permittivity values are above 16 (75% of the population of

329    MARSIS retrieved basal permittivity). It is interesting to note that only samples at 230K containing

330    at least 70% of nontronite fall inside this area.

331
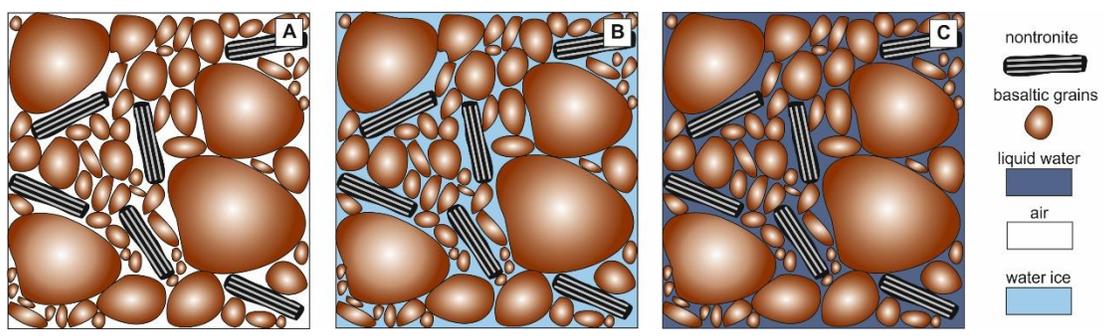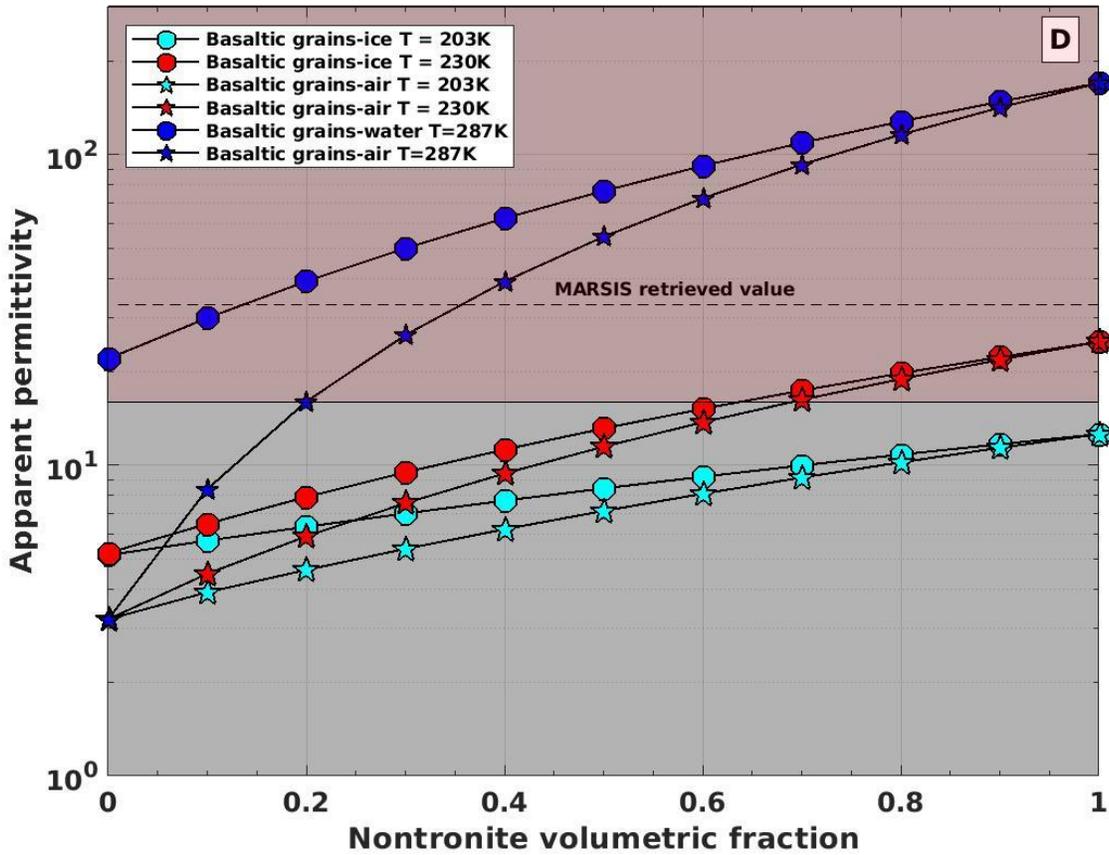
**Fig. 4** Effect of nontronite content on the apparent permittivity from CRIM simulations at 4 MHz. A) desiccated Martian model; B) water ice saturated Martian model; C) terrestrial analogue. D) Different colors and shapes indicate different temperatures and mixtures: dots represent ice or water saturated mixtures; stars are dry samples (with air-filled pores). The ratio between the volume fraction of the basaltic grains and the material in the pore is held constant (1.5), with the nontronite volume fraction progressively increasing. The black dashed line indicates the MARSIS threshold value $\varepsilon_a = 33$; pink area highlights the apparent permittivity interval for which the probability that the permittivity assumes values $\varepsilon_a \geq 16$ is 75%.

## 6. Laboratory dielectric measurements

### 6.1 Martian clay sediments analogs

We complemented literature data with new experimental results. We performed a set of laboratory measurements, selecting six clay samples collected in Italy in different geological settings: recent Holocene (< 12,000 years) fluvial deposits, Pliocene-Early Pleistocene (< 5 million years) marine mudstone, and metamorphic deposits dated from Jurassic to Oligocene (< 200 million years). The samples were mostly selected based on clay mineralogy (Table S1) which makes them good analogs for Martian clays (Fig. 1). The clay mineralogy and percentage of clay in the sediments were

determined by X-ray diffraction (XRD) (ref. to Fig.S1 and Appendix B) enabling us to directly compare our data with the analysis performed by the XRD instrument (CHEMIN) in Gale crater (Rampe et al. 2020a). We also considered the overall distribution of clays on Mars based on spectral investigations from orbiter to have a more global context and variability of Martian clays (Fig.1). Identified clay minerals in our samples are smectite, illite, kaolinite, and chlorite (only present in two samples) with variable quantities as also observed in Gale crater (ref. to Table S1; Fig. S1). The samples were sieved at 75μm and oven-dried at 105°C until their weight remained constant, and then rehydrated with distilled water until they returned to initial water content (13-31 wt%). For one clay sample we also collected a series of measurements for different water contents to evaluate the dielectric properties of clays at dry or low water content. Measurements were performed while the samples slowly warmed up from an initial temperature of 200 K, to ensure thermal equilibrium inside the sample during each frequency sweep. Real and imaginary parts as a function of frequency and temperature were measured using a coaxial transmission line and a Vector Network Analyzer (Mattei et al., 2013), in the frequency range 1 MHz-1 GHz and over the temperature interval 200 K – 298 K (Appendix C). Data are reported as apparent permittivity *vs*. temperature at 4 MHz (Fig. 5) to allow a direct comparison with the basal apparent permittivity retrieved by MARSIS (Orosei et al., 2018).

All clay samples show a similar trend: at 200 K the apparent permittivity ranges between 4.0 (Ch1) and 6.4 (Sm2) and slightly increases (curves almost parallel) up to 224 K, at which point the values start to diverge. At about 230 K, values of apparent permittivity range between 6 (Ch1) and 10 (Sm2). At 252 K, the sample Sm2 reaches MARSIS threshold value. The same threshold is reached by sample Sm3 at 258 K, samples Sm1 and Sm4 at 262 K and samples Ch1 and Ch2 at about 268 K. Above 265 K, ice melting produces a steep increase in the apparent permittivity, whereas above 273 K the trend changes to a gentler slope as ice is totally molten. At a temperature of 290 K the apparent permittivity reaches values ranging between $10^2$ - $10^3$, with Ch1 (13% water content, chlorite sample) being the lowest and Sm2 (21% water content, smectite sample) the highest. Moreover, the measurements collected on sample Sm4 at different water contents (Fig. S2) show that for low values of saturation (3.5% and 5.6% water content) the apparent permittivity at 273 K is around 10, reaching the MARSIS threshold value at 276 K with 14% of water content. No clear correlation between apparent permittivity and water content, clay content or clay mineralogy is recognizable in the data set (Fig.1 and Table S1), confirming the complexity of clay sediments dielectric behavior reported in the literature [e.g., Liu and Mitchell (2009), Lorek and Wagner (2013), Ishida (2002), Cadène et al. (2006)]. Moreover, data plotted as a function of frequency (Fig. S3) clearly show that both real and imaginary parts decrease when frequency increases, confirming

384  that in clay sediments caution should be taken when using values at 1 MHz to interpret radar data

385  collected at 4 MHz.

386
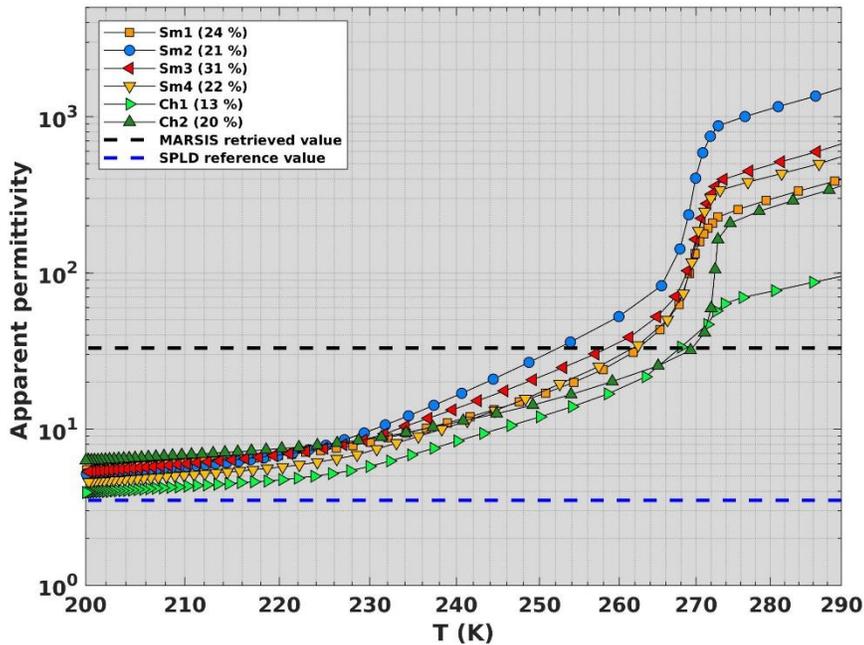


387

388  **Fig.5** Apparent permittivity at 4 MHz from experimental data. Apparent permittivity computed from real and imaginary

389  parts measured at 4 MHz as a function of temperature on four smectite-rich (Sm) and two chlorite-rich (Ch) sediments

390  having different water content (% in the legend). Black dashed line indicates the threshold $\varepsilon_a = 33$ retrieved by

391  MARSIS, and blue dashed line the SPLD ice permittivity value ($\varepsilon_1' = 3.5$) used to compute the apparent permittivity.

392  For clarity uncertainties are not shown in the diagram: they represent few percent of the measured values.

393

394  **6.2 Mg(ClO$_4$)$_2$ and CaCl$_2$ brines at Martian subglacial conditions**

395  Previous works (Orosei et al., 2018; Lauro et al., 2021) suggested brines as the most plausible cause

396  of MARSIS strong reflections as salty solutions can have very high complex permittivity (Addison,

397  1975). We quantify here the dielectric response of Mg(ClO$_4$)$_2$ and CaCl$_2$ brines at Martian

398  subglacial conditions by computing the apparent permittivity as a function of temperature at 4 MHz

399  from published (Stillman et al., 2010; Stillman and Grimm, 2011a; Grimm et al., 2008; Stillman

400  and Grimm, 2011b) and unpublished (measurement methodology is the same as Stillman et al.

401  (2010)) data. We considered pure solutions for high salt concentrations (Mg(ClO$_4$)$_2$ 44%wt, CaCl$_2$

402  33%wt, and CaCl$_2$ 21%wt) and both pure solutions and saturated sand for low salt concentrations

403  (100 mM for both Mg(ClO$_4$)$_2$ and CaCl$_2$). Measurements were taken between 180 K and 270 K,

404  noting however that, once the ice starts melting, the imaginary part dominates the measured signal,

405  and the real part cannot be measured accurately. Well below the eutectic temperature (216 K for

Mg(ClO$_4$)$_2$, and 222 K for CaCl$_2$) all saline solutions exhibit apparent permittivity values around 4, with the exception of the CaCl$_2$ at 33% (slightly hypereutectic) which is slightly higher (~ 5), probably due to the contribution of the salt grain inclusions in the ice [e.g., Pettinelli et al. (2016)] (Fig. 6A). These values indicate that, once a saline ice is completely frozen, the values of both real and imaginary parts are very low, and thus do not produce a strong dielectric contrast with the SPLD ice, irrespective of the concentration of salt. When the ice approaches the eutectic temperature, it starts to melt, generating an abrupt increase in both real and imaginary parts and in the apparent permittivity. At the eutectic temperature, for salt content around the eutectic concentration, the ice is largely or totally molten, and the apparent permittivity is higher than 10$^2$, well above the MARSIS threshold value (Fig. 6A). The volume fractions of the brines in each sample can be estimated from the eutectic temperature which is very close to the temperature where the curves intersect the threshold; we found 74% of brine content for CaCl$_2$ at 33%wt, 100% for Mg(ClO$_4$)$_2$ at 44%wt (eutectic concentration), and 44% for CaCl$_2$ at 21%wt. The dielectric response of the low concentration solutions is clearly different (Fig. 6B). Although an abrupt increase in apparent permittivity occurs around the eutectic temperature, its magnitude is much smaller: MARSIS threshold is reached by the pure CaCl$_2$ solution at ~240 K (Fig. 6B), and at higher temperatures by the other samples. The brine volume fractions at such temperatures are low (1.4 - 6.0%), but the high value of the apparent permittivity is justified as briny liquid vein networks form, which drastically increase the conductivity once the temperature of the sample is above that of the eutectic. Because salt is nearly insoluble in ice (Gross et al., 1977; Stillman et al., 2013), the salts and their resulting brines tend to concentrate along grain boundaries (Grimm et al., 2008).
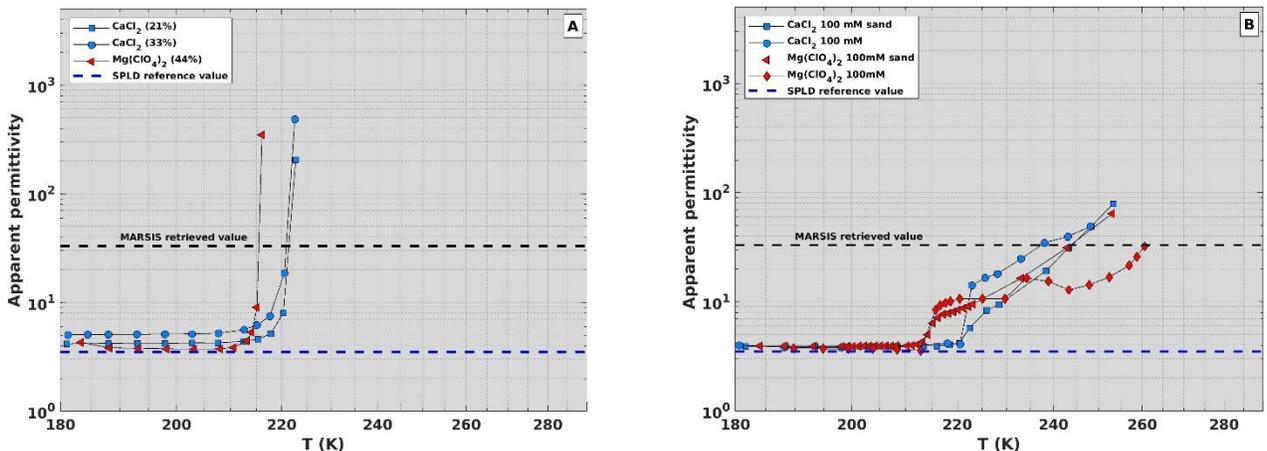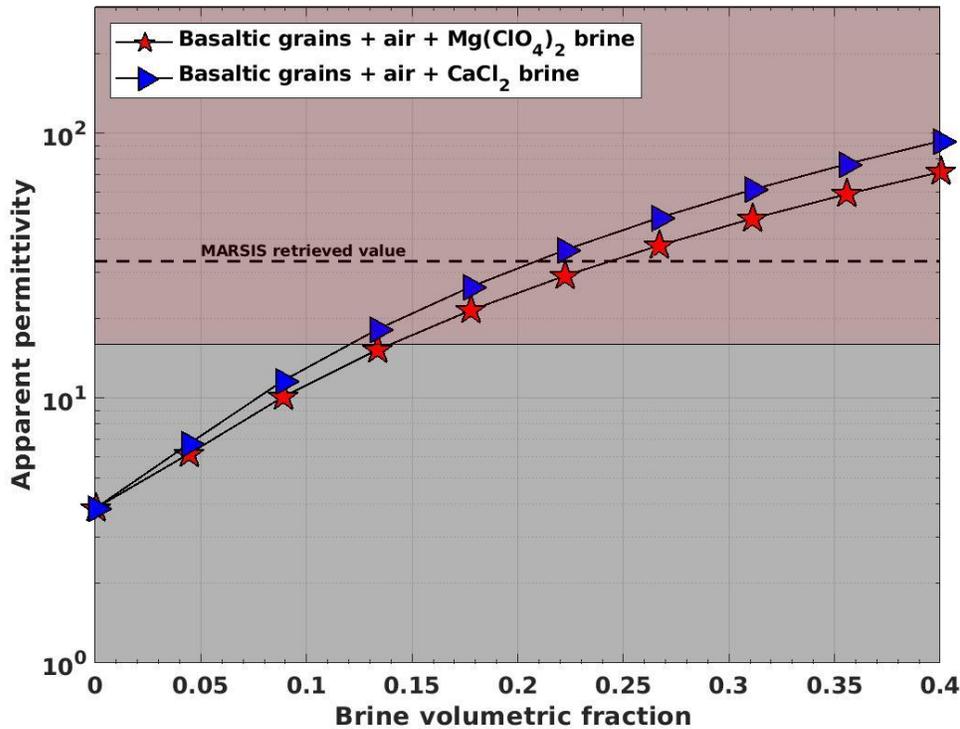
429    **Fig.6** Apparent permittivity of brines at 4 MHz as a function of temperature. A) Apparent permittivity of brine/ice

430    samples starting from 21% and 33%wt $CaCl_2$ and 44%wt $Mg(ClO_4)_2$ solutions. B) Apparent permittivity of $CaCl_2$ and

431    $Mg(ClO_4)_2$ salty ice/sand mixtures with 100 mM salt solutions. Two brine/ice samples with $CaCl_2$ and $Mg(ClO_4)_2$ and

432    two $CaCl_2$ and $Mg(ClO_4)_2$ ice/sand mixtures with 46% ($CaCl_2$) and 57.1% ($Mg(ClO_4)_2$) volumetric fraction of admixed

433    sand were measured. Black dashed line indicates the threshold $\varepsilon_a = 33$ retrieved by MARSIS, and blue dashed line the

434    SPLD ice permittivity value ($\varepsilon_1' = 3.5$) used to compute the apparent permittivity.

435

436    Finally, we used measured data and three-phases CRIM to evaluate the effect of eutectic or slightly

437    hypereutectic brine volume fractions on the overall apparent permittivity of a sandy soil (regolith)

438    (Fig. 7). For the complex permittivity of basaltic grains we used values from Mattei et al. (2014)

439    and for the brines those retrieved from $Mg(ClO_4)_2$ (44%wt) and $CaCl_2$ (33%wt) samples at the

440    eutectic temperature (Fig. 6A). The simulations compute the apparent permittivity of a soil with

441    pores progressively saturated with brines. Even though the $CaCl_2$ (33% wt) is not an exact eutectic

442    concentration, it is however close enough to produce reliable values. The results of the simulations

443    do not appreciably differ, with the MARSIS threshold value reached by sand/$CaCl_2$ brine mixtures

444    at about 21% of brines volume fraction, and by sand/$Mg(ClO_4)_2$ brine mixture at about 25% (Fig.

445    7). Note that for brines volume fraction higher than 15% the apparent permittivity is above 16 (pink

446    area in Fig.7). For a fully saturated soil (40% porosity) the apparent permittivity of the sand/$CaCl_2$

447    brine mixtures is ~94 and for the sand/$Mg(ClO_4)_2$ brine mixture it is close to 71.

**Fig.7** Effect of brines contents on the apparent permittivity of a soil from CRIM simulations at 4MHz. Apparent permittivity computed for a sandy soil with 40% porosity, from dry to brines saturated conditions. Blue triangles (33%wt CaCl$_2$) refer to the apparent permittivity measured at ~222K and red stars (44%wt Mg(ClO$_4$)$_2$) to the apparent permittivity measured at ~216K. Black dashed line indicates the threshold $\varepsilon_a = 33$ retrieved by MARSIS; pink area highlights the apparent permittivity interval for which the probability that the permittivity assumes values $\varepsilon_a \geq 16$ is 75%.

## 7. Discussion and Conclusion

Data collected by MARSIS and SHARAD in the areas where hydrated minerals have been found and/or where they are particularly abundant (Fig.1), do not show any indication of bright reflections coming from the surface. Given the cold temperatures and low water content estimated on Mars (2.3–3.1 wt.% H$_2$O) (Thomas et al., 2020), clay minerals have been considered a concern for radar attenuation but not a strong surface reflector, capable of preventing radar signals penetrating through the surface (Stillman and Grimm, 2011a; Cunje et al., 2018). These observations are in good agreement with literature data (Ca-bentonite sample in Fig. 3) and with our experimental results (Fig. S2), which show that hydrated salts and dry or low water content clay, do not generate strong radar reflections on the Martian surface or at the base of the SPLD (Table 1). Consequently, even if present in large amount in the basal sediments, hydrated salts and dry clay would exhibit apparent permittivity similar or of even lower than the SPLD ice (see Fig.S2).

466    Temperature has a dominating effect on the dielectric properties of clay and clay sediments (Lorek

467    and Wagner, 2013; Moore and Maeno, 1993; Bittelli et al., 2004). High values (25.1), such as those

468    shown at 230 K by almost pure nontronite (21% water content), are reduced by half (12.6) when

469    the temperature drops to 203 K. At this temperature, a clay sediment containing 60% of nontronite

470    does not exceed an apparent permittivity value of 9 (Fig. 4D). The drastic effect of temperature on

471    the dielectric behavior of clays is confirmed by our set of measurements conducted on clay

472    sediments at different water content, clay content, and different mineralogy: the MARSIS threshold

473    value is only obtained at high temperature ($\geq$ 250K). At 203 K the apparent permittivity of the clay

474    sediments does not exceed 7, a value not dissimilar from the apparent permittivity values reported

475    for the hydrated salts or dry clay (Table 1). Comparing published data, simulations, and laboratory

476    measurements, we found that at 4 MHz and 230 K, the apparent permittivity of clay sediments,

477    even with a very high percentage of clay (70% volume fraction of nontronite) barely exceeds 16,

478    while at 203 K it does not go beyond 10. It follows that very low temperatures, such as those

479    commonly inferred at the base of the SPLD ($\leq$ 200K), are totally inconsistent with the hypothesis

480    that clay sediments can generate a dielectric contrast with the SPLD large enough to obtain bright

481    basal echoes.

482    Our dielectric measurements on $Mg(ClO_4)_2$ and $CaCl_2$ brines at Martian subglacial conditions rule

483    out also salty ice as the cause for MARSIS bright reflections. Totally frozen brines having high

484    concentration of salts exhibit very low apparent permittivity, because salt grain inclusions do not

485    appreciably change the dielectric properties of the ice at MARSIS frequencies (Fig. 6A). These

486    results are supported by published data on the dielectric properties of sea ice at very low temperature

487    [e.g., Addison (1975), Fujino (1967)]. The apparent permittivity at low salt concentration (100 mM)

488    does not exceed 10-15 at the eutectic temperature. However, our results (Fig. 6B) suggest that a

489    few 100s mM of salt would probably be enough to reach the MARSIS threshold value (Stillman et

490    al., 2021). Vice versa, given the very large apparent permittivity values measured for both

491    $Mg(ClO_4)_2$ and $CaCl_2$ brines at high salt concentrations (Fig. 6A), a few 10s percent of liquid brine

492    volume fraction in the ice or in the soil would probably be sufficient to enhance the overall apparent

493    permittivity well above the MARSIS retrieved value (Fig.6A and Fig.7). Thus, based on their

494    dielectric behavior alone, $Mg(ClO_4)_2$ and $CaCl_2$ brines appear to be the preferable candidates to

495    explain MARSIS bright basal reflections observed in Ultimi Scopuli (Orosei et al., 2018; Lauro et

496    al., 2021). It has been argued that the eutectic temperatures of brines are too high to explain the

497    presence of liquid water at the base of the SPLD (Sori and Bramson, 2019). Previous studies have

498    found that salts with large freezing point depressions also have large metastable eutectic

499    temperatures that can be 10s of degrees lower than their eutectic temperature (Toner and Catling,

500  2018; Primm et al., 2020). Our measurements were performed after freezing the salt solutions to

501  much colder temperature (<188 K) than the eutectic temperatures. For example, the 100 mM

502  Mg(ClO$_4$)$_2$ sample was held at 193 K for 72 hours and never fully froze, until the temperature was

503  reduced to 188 K. We can expect that other perchlorates like Ca(ClO$_4$)$_2$ (eutectic temperature ~198

504  K) would exhibit a dielectric response similar to the salts investigated in this work, but at lower

505  temperature. Additionally, it has been proven that a mixture of Ca and Mg perchlorate has eutectic

506  temperature well below those of the single salts (Nair and Unnikrishnan, 2020) and the brines can

507  remain in a supercooled state at temperatures as low as 150 K (Toner et al., 2014). Whether

508  supercooled salty waters can persist in subglacial environments over geologic timescales is still an

509  open issue. Future work will need to focus on the specific question of the longevity of brines in

510  hyperarid cold conditions. Metastability aside, however, another poorly constrained parameter is

511  the thermal conductivity of the SPLD deposits, which directly bears on estimated values of basal

512  temperatures: Sori and Bramson (2019) argue that under the current (and most likely) value of heat

513  flux at the south polar region of Mars, the temperature at the base of the SPLD in Ultimi Scopuli is

514  < 180 K. However, their model involves a highly conductive SPLD, which is far from being

515  conclusively demonstrated. In fact, small variations in estimated values of conductivity of the SPLD

516  materials, could dramatically increase basal temperatures to values equal to or even above those of

517  perchlorate brine eutectics.

518

519

520

521

522  **Appendix A**

523  The absolute value of the reflection coefficient $\Gamma_{12}$ can be rewritten as:

524  $$\left|\Gamma_{12}\right| = \left|\frac{\sqrt{\varepsilon_2} - \sqrt{\varepsilon_1}}{\sqrt{\varepsilon_2} + \sqrt{\varepsilon_1}}\right| \quad (6)$$

525  The complex permittivity of the second medium can be expressed in terms of its module and

526  phase as:

527  $$\varepsilon_2 = \varepsilon_2' + i\varepsilon_2'' = \left|\varepsilon_2\right|e^{i\theta} = \left|\varepsilon_2\right|(\cos\theta + i\sin\theta) \quad (7)$$

528  With

$$\cos\theta = \frac{\varepsilon_2{}'}{|\varepsilon_2|}$$

$$\sin\theta = \frac{\varepsilon_2{}''}{|\varepsilon_2|}$$

530    As a consequence, using the bisection rules, the square root of $\varepsilon_2$ is given by:

531    $$\sqrt{\varepsilon_2} = \sqrt{|\varepsilon_2|}\,e^{i\frac{\theta}{2}} = \sqrt{|\varepsilon_2|}\left(\cos\frac{\theta}{2} + i\sin\frac{\theta}{2}\right) = \sqrt{|\varepsilon_2|}\left(\sqrt{\frac{1+\cos\theta}{2}} + i\sqrt{\frac{1-\cos\theta}{2}}\right)$$

532    Replacing the last equation in Equation 6 we have:

533    $$|\Gamma_{12}| = \left|\frac{\sqrt{|\varepsilon_2|}\sqrt{1+\cos\theta} - \sqrt{2\varepsilon_1} + i\sqrt{|\varepsilon_2|}\sqrt{1-\cos\theta}}{\sqrt{|\varepsilon_2|}\sqrt{1+\cos\theta} + \sqrt{2\varepsilon_1} + i\sqrt{|\varepsilon_2|}\sqrt{1-\cos\theta}}\right| \quad (8)$$

534    The absolute value of $\Gamma_{12}$ is given by,

535
$$|\Gamma_{12}| = \sqrt{\frac{\left(\sqrt{|\varepsilon_2|}\sqrt{1+\cos\theta} - \sqrt{2\varepsilon_1}\right)^2 + \left(\sqrt{|\varepsilon_2|}\sqrt{1-\cos\theta}\right)^2}{\left(\sqrt{|\varepsilon_2|}\sqrt{1+\cos\theta} + \sqrt{2\varepsilon_1}\right)^2 + \left(\sqrt{|\varepsilon_2|}\sqrt{1-\cos\theta}\right)^2}} =$$

$$= \sqrt{\frac{|\varepsilon_2|(1+\cos\theta) - 2\sqrt{2\varepsilon_1|\varepsilon_2|}\sqrt{1+\cos\theta} + 2\varepsilon_1 + |\varepsilon_2|(1-\cos\theta)}{|\varepsilon_2|(1+\cos\theta) + 2\sqrt{2\varepsilon_1|\varepsilon_2|}\sqrt{1+\cos\theta} + 2\varepsilon_1 + |\varepsilon_2|(1-\cos\theta)}} = \quad (9)$$

$$= \sqrt{\frac{|\varepsilon_2| - \sqrt{2\varepsilon_1|\varepsilon_2|}\sqrt{1+\cos\theta} + \varepsilon_1}{|\varepsilon_2| + \sqrt{2\varepsilon_1|\varepsilon_2|}\sqrt{1+\cos\theta} + \varepsilon_1}} = \frac{\sqrt{|\varepsilon_2|^2 + \varepsilon_1{}^2 - 2\varepsilon_1|\varepsilon_2|\cos\theta}}{|\varepsilon_2| + \varepsilon_1 + \sqrt{2\varepsilon_1|\varepsilon_2|}\sqrt{1+\cos\theta}}$$

536    Now, we want to estimate $\varepsilon_a$ that is the quantity for which we can write the reflection coefficient

537    like a real quantity, i.e.:

538    $$|\Gamma_{12}| = \frac{\sqrt{\varepsilon_a} - \sqrt{\varepsilon_1}}{\sqrt{\varepsilon_a} + \sqrt{\varepsilon_1}} \quad (10)$$

539    From equation (10) it follows:

540    $$\varepsilon_a = \varepsilon_1 = \left(\frac{1+|\Gamma_{12}|}{1-|\Gamma_{12}|}\right)^2 = \varepsilon_1 \frac{1+|\Gamma_{12}|^2 + 2|\Gamma_{12}|}{1+|\Gamma_{12}|^2 - 2|\Gamma_{12}|} \quad (11)$$

541    From equation (9) we can calculate $|\Gamma_{12}|^2$:

542 $$\left|\Gamma_{12}\right|^2 = \frac{\varepsilon_1 + \left|\varepsilon_2\right| - \sqrt{2\varepsilon_1\left|\varepsilon_2\right|}\sqrt{1+\cos\theta}}{\varepsilon_1 + \left|\varepsilon_2\right| + \sqrt{2\varepsilon_1\left|\varepsilon_2\right|}\sqrt{1+\cos\theta}} \quad (12)$$

543 It follows that

544 $$1 + \left|\Gamma_{12}\right|^2 \pm 2\left|\Gamma_{12}\right| = 2\frac{\varepsilon_1 + \left|\varepsilon_2\right| \pm \sqrt{\left|\varepsilon_2\right|^2 + \varepsilon_1^2 - 2\varepsilon_1\left|\varepsilon_2\right|\cos\theta}}{\varepsilon_1 + \left|\varepsilon_2\right| + \sqrt{2\varepsilon_1\left|\varepsilon_2\right|}\sqrt{1+\cos\theta}} \quad (13)$$

545 Replacing equation (13) in equation (10), we obtain:

$$\varepsilon_a = \varepsilon_1 \frac{\dfrac{\varepsilon_1 + \left|\varepsilon_2\right| + \sqrt{\left|\varepsilon_2\right|^2 + \varepsilon_1^2 - 2\varepsilon_1\left|\varepsilon_2\right|\cos\theta}}{\varepsilon_1 + \left|\varepsilon_2\right| + \sqrt{2\varepsilon_1\left|\varepsilon_2\right|}\sqrt{1+\cos\theta}}}{\dfrac{\varepsilon_1 + \left|\varepsilon_2\right| - \sqrt{\left|\varepsilon_2\right|^2 + \varepsilon_1^2 - 2\varepsilon_1\left|\varepsilon_2\right|\cos\theta}}{\varepsilon_1 + \left|\varepsilon_2\right| + \sqrt{2\varepsilon_1\left|\varepsilon_2\right|}\sqrt{1+\cos\theta}}} =$$

546 $$= \varepsilon_1 \frac{\varepsilon_1 + \left|\varepsilon_2\right| + \sqrt{\left|\varepsilon_2\right|^2 + \varepsilon_1^2 - 2\varepsilon_1\left|\varepsilon_2\right|\cos\theta}}{\varepsilon_1 + \left|\varepsilon_2\right| - \sqrt{\left|\varepsilon_2\right|^2 + \varepsilon_1^2 - 2\varepsilon_1\left|\varepsilon_2\right|\cos\theta}} =$$

$$= \varepsilon_1 \frac{\varepsilon_1 + \left|\varepsilon_2\right| + \sqrt{\varepsilon_1^2 + \left|\varepsilon_2\right|^2 - 2\varepsilon_1\varepsilon_2'}}{\varepsilon_1 + \left|\varepsilon_2\right| - \sqrt{\varepsilon_1^2 + \left|\varepsilon_2\right|^2 - 2\varepsilon_1\varepsilon_2'}}$$

547 That is the expression of the apparent permittivity given in equation (5).

548

549 **Appendix B**

550 **X-ray Diffraction analysis (XRD)**

551 Mineralogical analysis was performed using the Rigaku MiniFlex II X-ray diffractometer with Cu-

552 Ka radiation, monochromated with graphite and operated at 30 kV and 15 mA. The diffraction

553 pattern was acquired on bulk powder samples obtained by grinding small pieces of rock with

554 mechanical agata mortar and pestle. The XRD patterns were collected in the 3–50 2θ range which

555 is representative of the main mineral species diffraction peaks. The different mineralogical species

556 were identified by matching the peaks with the reference Crystallography Open Database (COD

557 2020) using the Match! software (version 3.10.2). Semi-quantitative analysis was performed using

558 a Reference Intensity Ratio method (RIR-method) included in the Match! software (version 3.10.2).

559 This analysis is based on I/Ic factor indicating the ratio between the intensity of the highest peak

560 diffraction of the identified phase in comparison with the highest peak of Corundum standard.

561

**Appendix C**

**Dielectric measurements**

The experimental set-up consists of a two-port Vector Network Analyzer (Agilent E5071C) connected through two cables to a coaxial-cage line (cell) filled with the material under test. The measuring cell is a stainless-steel cage housed in a plexiglass box; it consists of a central conductor and an outer structure made by eight equally spaced rods arranged in a cylindrical pattern. Detailed description of the setup can be found elsewhere (Mattei et al., 2013). The experimental setup allows to retrieve the dielectric properties of the material under test (in terms of complex dielectric permittivity and complex magnetic permeability), applying the Nicolson-Ross-Weir algorithm (Nicolson and Ross, 1970; Weir, 1974). The fundamental equations are given by:

$$\sqrt{\frac{\varepsilon}{\mu}} F_g = \frac{1-\Gamma}{1+\Gamma} \quad (14)$$

$$\sqrt{\varepsilon \mu} l = \frac{jc}{2\pi f} \ln(\Psi) \quad (15)$$

where $\Gamma$ and $\Psi$ are the reflection and transmission coefficients through the coaxial line, $\varepsilon$ and $\mu$ are the complex relative dielectric permittivity and magnetic permeability, respectively, $F_g$ is a geometrical factor that accounts for the impedance mismatch between the coaxial cables and the coaxial-cage line in air, $l$ is the length of the coaxial-cage line and $c$ is the velocity of the light in a vacuum. Combining Equation (14) and (15), the complex dielectric permittivity can be retrieved as follows:

$$\varepsilon = \frac{jc}{2\pi f} \frac{1}{F_g l} \frac{1-\Gamma}{1+\Gamma} \ln(\Psi) \quad (16)$$

The coaxial-cage line is inserted in a cryostat and cooled using dry ice pellets. The measurements were performed first progressively decreasing the temperature from 298 K to 200 K and then allowing the system to slowly reach room temperature. Each cycle lasted about 50 h, 10 h for cooling and 40 h for heating the sample. A Pt-100 probe was inserted in the coaxial-cage line to measure sample temperature during the entire cycle.

592   **Appendix D**

593   Supplementary material

594

595   **References**

596   Addison J. R., Electrical properties of saline ice at 1 kHz down to− 150° C. *J. App. Phys.*, **46**(2),

597     513-522 (1975).

598   Bibring J.P., Y. Langevin, J.F. Mustard, F. Poulet, R. Arvidson, A. Gendrin, B. Gondet, N.

599     Mangold, P. Pinet, P. Forget, Global mineralogical and aqueous Mars history derived from

600     OMEGA/Mars Express data. *Science* **312**, 400–404 (2006).

601   Bierson C. J., S. Tulaczyk, S. W. Courville, N. E. Putzig, Strong MARSIS Radar Reflections

602     from the Base of Martian South Polar Cap may be due to Conductive Ice or Minerals.

603     *Geophysical Research Letters*, e2021GL093880 (2021).

604   Bishop J.L., A.G. Fairèn, J.R. Michalski, L. Gago-Duport, L.L. Baker, M. A. Velbel, C., Gross,

605     E.B. Rampe, Surface clay formation during short-term-warmer and wetter conditions on largely

606     cold ancient Mars. *Nature Astronomy* **2**, 206-2013 (2018).

607   Bittelli M., M. Flury, K. Roth Use of dielectric spectroscopy to estimate ice content in frozen

608     porous media. *Water resources research*, **40**(4) (2004).

609   Bristow T.F., E.B. Rampe, C.N. Achilles, D.F. Blake, S.J. Chipera, P. Craig, J.A. Crisp, D.J.

610     Des Marais, R.T. Downs, R. Gellert, J.P. Grotzinger, S. Gupta, R.M. Hazen, B. Horgan, J.V.

611     Hogancamp, P.R. Mahaffy, A.C. McAdam, D.W. Ming, J.M. Morookian, R.V. Morris, S.M.

612     Morris, A. H. Treiman, D.T. Vaniman, A.R. Vasavada, A.S. Yen, Clay Mineral Diversity and

613     Abundance in Sedimentary Rocks of Gale Crater, Mars. *Sci. Adv*. **4**, eaar3330 (2018).

614   Burton E. F., L. G. Turnbull, Dielectric constants of solids at high frequencies and the influence

615     of water of crystallization on dielectric constant. Proceedings of the Royal Society of London.

616     Series A-Mathematical and Physical Sciences, 158(893), 182-198 (1937).

617   Cadène A., B. Rotenberg, S. Durand-Vidal, J. C. Badot, P. Turq, Dielectric spectroscopy as a

618     probe for dynamic properties of compacted smectites. *Physics and Chemistry of the Earth, Parts

619     A/B/C*, **31**(10-14), 505-510 (2006).

620   Chelidze T. L., Y. Gueguen, C. Ruffet, Electrical spectroscopy of porous rocks: a review—II.

621     Experimental results and interpretation. *Geophysical Journal International*, **137**(1), 16-34

622     (1999).

623   Cheng C. K., The dielectric constants of some metallic sulphates containing various amounts of

624     water of crystallization. *The London, Edinburgh, and Dublin Philosophical Magazine and

625     Journal of Science*, **30**(203), 505-515 (1940).

Chevrier V. F., J. Hanley, T. S. Altheide, Stability of perchlorate hydrates and their liquid solutions at the Phoenix landing site, Mars. *Geophys. Res. Lett.*, **36**(10) (2009).

Clark B.C., R.E. Arvidson, R. Gellert, R.V. Morris, D.W. Ming, L. Richter, S.W.Ruff, , J.R. Michalski, W.H. Ferrand, A.Yen, K.E. Herkenhoff, R. Li, S.W. Squyres, C. Schröder, G. Klingelhöfer, J.F. Bell III, Evidence for montmorillonite or its compositional equivalent in Columbia Hills, Mars. *J. Geophys. Res.* **112**, E06S01 (2007).

Cunje A. B., R. R. Ghent, A. Boivin, C. A. Tsai, D. Hickson, Dielectric properties of Martian regolith analogs and smectite clays. In Lunar and Planetary Science Conference (No. **2083**, p. 1805) (2018).

Ehlmann B. L., J. F. Mustard, S. L. Murchie, J.P. Bibring, A. Meunier, A. Fraeman, Y. Langevin, Subsurface water and clay mineral formation during the early history of Mars, *Nature* **479**,53–60 (2011).

Ehlmann B. L., J.F. Mustard, G.A. Swayze, R.N. Clarck, J.L. Bishop, F. Poulet, D.J. Des Marais, L. H. Roach, R. E. Milliken, J.J. Wray, O. Barnouin-Jha, S.L. Murchie, Identification of hydrated silicate minerals on Mars using MRO-CRISM: Geologic context near Nili Fossae and implications for aqueous alteration. *Journal of Geophysical Research* **114**, E00D08, (2009).

Ehlmann B.L., C.S. Edwards, Mineralogy of the Martian surface. *Annu Rev Earth Planet Sci* **42**, 291-315 (2014).

Ehlmann B.L., G. Berger, N. Mangold, J.R. Michalski, D.C. Catling, S.V. Ruff, E. Chassefière, P.B. Niles, V. Chevrier, F. Poulet, Geochemical consequences of widespread clay mineral formation in Mars'Ancient Crust. *Space Science Review* **174**, 329–364 (2013).

Fujino K., Electrical properties of sea ice. *Phys. of Snow and Ice: proc.* **1**(1), 633-648 (1967).

Gaudin A., E. Dehouck, O. Grauby, N. Mangold, Formation of clay minerals on Mars: Insights from long-term experimental weathering of olivine. *Icarus*, **311**, 210-223 (2018).

Gooding J.L., D.W. Muenow, Martian volatiles in shergottite EETA 79001: New evidence from oxidized sulfur and sulfur-rich aluminosilicates. *GCA* **50**(6), 1049-1059 (1986).

Grima C., J. S. Greenbaum, E. J. Lopez Garcia, K. M. Soderlund, A. Rosales, D. D. Blankenship, D. A.Young, Radar detection of the brine extent at McMurdo Ice Shelf, Antarctica, and its control by snow accumulation. *Geophysical Research Letters*, **43**(13), 7011-7018 (2016).

Grimm R. E., D. E. Stillman, S. F. Dec, M. A. Bullock, Low-frequency electrical properties of polycrystalline saline ice and salt hydrates. *J. Phys. Chem.* B **112**(48), 15382-15390 (2008).

Gross G.W., P.M. Wong, K. Humes, Concentration dependent solute redistribution at the ice-water phase boundary. III. Spontaneous convection. Chloride solutions. *J. Chem. Phys.* **67**(11), 5264–5274 (1977).

Ishida T., Dielectric Behavior of Clay Surfaces. Encyclopedia of Surface and Colloid, *Science*, 1385-1392 (2002).

Johnston C. T., Probing the nanoscale architecture of clay minerals. *Clay Minerals*, **45**(3), 245-279 (2010).

Kaatze U., Complex permittivity of water as a function of frequency and temperature. *J. Chem. Engin. Data* **34**(4), 371-374 (1989).

Kaden H., F. Königer, M. Strømme, G. A. Niklasson, K. Emmerich, Low-frequency dielectric properties of three bentonites at different adsorbed water states. *Journal of colloid and interface science*, **411**, 16-26 (2013).

Kamiyoshi K. I., T. Miyamoto, Dielectric properties of the water of crystallization. In Science Reports of the Research Institutes, Tohoku University. Ser. A, Physics, Chemistry and Metallurgy, Vol. 2, pp. 370-379, (1950).

Kao K. C., Dielectric phenomena in solids. Elsevier (2004).

Kaviratna P. D., T. J. Pinnavaia, P. A. Schroeder, Dielectric properties of smectite clays. *Journal of Physics and Chemistry of Solids*, **57**(12), 1897-1906 (1996).

Kounaves S.P., B.L. Carrier, G.D. O'Neil, S.T. Stroble, M.W. Claire Evidence of martian perchlorate, chlorate, and nitrate in Mars meteorite EETA79001: Implications for oxidants and organics. *Icarus* **229**, 206-213 (2014).

Kułacz K., J. Waliszewski, S. Bai, L. Ren, H. Niu, K. Orzechowski, Changes in structural and dielectric properties of nontronite caused by heating. *Applied Clay Science*, **202**, 105952 (2021).

Kułacz K., K. Orzechowski, Nontronite and intercalated nontronite as effective and cheap absorbers of electromagnetic radiation. *Dalton Transactions*, **48**(12), 3874-3882 (2019).

Kuligiewicz A., A. Derkowski, Tightly bound water in smectites. *American Mineralogist*, **102**(5), 1073-1090 (2017).

Lauro S. E., E. Pettinelli, G. Caprarelli, L. Guallini, A. P. Rossi, E. Mattei, R. Orosei, Multiple subglacial water bodies below the south pole of Mars unveiled by new MARSIS data. *Nat. Astron.*, **5**(1), 63-70 (2021).

Leshin L.A., E. Vicenzi, Aqueous processes recorded by Martian meteorites: Analyzing Martian water on Earth. *Elements* **2**(3), 157-162 (2006).

Liu N., J. K. Mitchell, Modelling electromagnetic properties of saturated sand and clay. *Geomechanics and Geoengineering: An International Journal*, **4**(4), 253-269 (2009).

Lorek A., N. Wagner, Supercooled interfacial water in fine-grained soils probed by dielectric spectroscopy. *The Cryosphere*, **7**(6), 1839-1855 (2013).

Mattei E., S. E. Lauro, E. Pettinelli, G. Vannaroni, Coaxial-Cage Transmission Line for Electromagnetic Parameters Estimation. *IEEE Trans. Instr. Meas.* **62**, (2013).

Mattei E., S. E. Lauro, G. Vannaroni, B. Cosciotti, F. Bella, E. Pettinelli, Dielectric measurements and radar attenuation estimation of ice/basalt sand mixtures as martian Polar Caps analogues. *Icarus* **229**, 428-433 (2014).

McSween H.Y., What we have learned about Mars from SNC meteorites. *Meteoritics* **29**, 757-779 (1994).

Moore J. C., N. Maeno, Dielectric properties of frozen clay and silt soils. *Cold regions science and technology*, **21**(3), 265-273 (1993).

Murchie S.L., J.F. Mustard, B.L. Ehlmann, R.E. Milliken, J.L. Bishop, N.K. McKeown, D.J. Noe Dobrea EZ, F.P. Seelos, D.L. Buczkowski, S.M. Wiseman, R.E. Arvidson, J.J. Wray, G. Swayze, R.N. Clark, Des Marais, A.S. McEwen, J.P. Bibring, A synthesis of Martian aqueous mineralogy after 1 Mars year of observations from the Mars Reconnaissance Orbiter. *J Geophys Res Planets* **114**, E00D06 (2009).

Murchie S.L., R. Arvidson, P. Bedini, K. Beisser, J.P. Bibring, J. Bishop, J. Boldt, P. Cavender, , T. Choo, R.T. Clancy, E.H. Darlington, D. Des Marais, R. Espiritu, D. Fort, R. Green, E. Guinness, J. Hayes, C. Hash, K. Heffernan, J. Hemmler, G. Heyler, D. Humm, J. Hutchison, N. Izenberg, R. Lee, J. Lees, D. Lohr, E. Malaret, T. Martin, J.A. McGovern, P. McGuire, R. Morris, J. Mustard, S. Pelkey, E. Rhodes, V. Robinson, T. Roush, E. Schaefer, G. Seagrave, F. Seelos, P. Silverglate, S. Slavney, M. Smith, W. J. Shyong, K. Strohbehn, H. Taylor, P. Thompson, B. Tossman, M. Wirzburger, M. Wolff, Compact Reconnaissance Imaging Spectrometer for Mars (CRISM) on Mars Reconnaissance Orbiter (MRO). *J. Geophys. Res.* **112**, E05S03 (2007).

Mustard J.F., C.D. Cooper, M.K. Rifkin, Evidence for recent climate change on Mars from the identification of youthful near-surface ground ice. *Nature* **412**, 411-414 (2001).

Muttik N., F.M. McCubbin, L.P. Keller, A.R. Santos, W.A. McCutcheon, P.P. Provencio, Z. Rahman, C.K. Shearer, J.W. Boyce, C.B. Agee Inventory of H2O in the ancient Martian regolith from Northwestern Africa 7034: The important role of Fe oxides. *Geophys Res Lett.* **41**(23), 8235-8244 (2014).

Nair C. R., V. Unnikrishnan, Stability of the Liquid Water Phase on Mars: A Thermodynamic Analysis Considering Martian Atmospheric Conditions and Perchlorate Brine Solutions. *ACS omega* **5**(16), 9391-9397 (2020).

Nicolson A. M., G. F. Ross, Measurement of the intrinsic properties of materials by time-domain techniques. *IEEE Trans. Instr. Meas.* **19**(4), 377-382 (1970).

Nobes D. C., E. F. Davis, S. A. Arcone, "Mirror-image" multiples in ground-penetrating radar. *Geophysics*, **70**(1), K20-K22 (2005).

Olhoeft G. R., Electrical properties of natural clay permafrost. Canadian Journal of Earth *Sciences*, **14**(1), 16-24 (1977).

Olhoeft G. R., Electrical properties of rocks. *Physical properties of rocks and minerals*, **2**, 257-297 (1981).

Olhoeft G. R., Tables of room temperature electrical properties for selected rocks and minerals with dielectric permittivity statistics. US Department of the Interior, *Geological Survey* (1979).

Orosei R., S. E. Lauro, E. Pettinelli, A. Cicchetti, M. Coradini, B. Cosciotti, R. Seu, Radar evidence of subglacial liquid water on Mars. *Science*, **361**(6401), 490-493 (2018).

Parkhomenko E. I., Electrical Properties of Rocks (1967).

Pettinelli E., S. E. Lauro, B. Cosciotti, E. Mattei, F. Di Paolo, G. Vannaroni, Dielectric characterization of ice/MgSO4· 11H2O mixtures as Jovian icy moon crust analogues. *Earth and Planetary Science Letters*, **439**, 11-17 (2016).

Plesa A.C., S. Padovan, N. Tosi, D. Breuer, M. Grott, M.A. Wieczorek, T. Spohn, S.E. Smrekar, W.B. Banerdt, The thermal state and interior structure of Mars. *Geophys. Res. Lett.* **45**, 12198-12209, (2018).

Poulet F., D. Mangold, D. Loizeau, J.P. Bibring, Y. Langevin, J. Michalski, B. Gondet, Abundance of minerals in the phyllosilicate-rich units on Mars. *Astron. Astrophys* **487**, L41–L44 (2008).

Primm K. M., D. E. Stillman, T. I. Michaels, Investigating the hysteretic behavior of Mars-relevant chlorides. *Icarus* **342**, 113342 (2020).

Rampe E. B., D. W. Ming, D. F. Blake, T. F. Bristow, S. J. Chipera, J. P. Grotzinger, R. V. Morris, S. M. Morrison, D. T. Vaniman, A. S. Yen, C. N. Achilles, P. I. Craig, D. J. Des Marais, R. T.Downs, J. D. Farmer, K. V. Fendrich, R. Gellert, R. M. Hazen, L. C. Kah, J. M. Morookian, T. S. Peretyazhko, P. Sarrazin, A. H. Treiman, J. A. Berger, J. Eigenbrode, A. G. Fairén, O. Forni, S. Gupta, J. A. Hurowitz, N. L. Lanza, M. E. Schmidt, K. Siebach. B. Sutter, L. M. Thompson, Mineralogy of an ancient lacustrine mudstone succession from the Murray formation, Gale crater, Mars. *Earth and Plan. Science Lett.* **471**, 172-185 (2017).

Rampe E. B., D.F. Blake, T.F. Bristow, D.W. Ming, D.T. Vaniman, R.V. Morris, C.N. Achilles, S.J. Chipera, S.M. Morrison, V.M. Tu, A.S. Yen, N. Castle, G.W. Downs, R.T. Downs, J.P. Grotzingere, R.M. Hazen, A.H. Treiman, T.S. Peretyazhko, D.J. Des Marais, R.C. Walroth, P.I. Craig, J.A. Crisp, B. Lafuente, J.M. Morookian, P.C. Sarrazin, M.T. Thorpe, J.C. Bridges, L.A. Edgar, C.M. Fedo, C. Freissinet, R. Gellert, P.R. Mahaffy, H.E. Newsom, J.R. Johnson, L.C.

Kah, K.L. Siebach, J. Schieber, V.Z. Sun, A.R. Vasavada, D. Wellington, R.C. Wiens, Mineralogy and geochemistry of sedimentary rocks and eolian sediments in Gale crater, Mars: A review after six Earth years of exploration with Curiosity. *Geochemistry* **80** ,125605 (2020a).

Rampe E. B., T. F. Bristow, R. V. Morris, S. M. Morrison, C. N. Achilles, D. W. Ming, D. T. Vaniman, D. F. Blake, V. M. Tu, S. J. Chipera, A. S. Yen, T. S. Peretyazhko, R. T. Downs, R. M. Hazen, A. H. Treiman, J. P. Grotzinger, N. Castle, P. I. Craig, D. J. Des Marais, M. T. Thorpe, R. C. Walroth, G. W. Downs, A. A. Fraeman, K. L. Siebach, R. Gellert, A. C. McAdam, P. -Y. Meslin, B. Sutter, M. R. Salvatore, Mineralogy of Vera Rubin Ridge from the Mars Science Laboratory CheMin Instrument. *J. Geophys. Res.* **125**, e2019JE006306. (2020b).

Rutishauser A., D. D. Blankenship, M. Sharp, M. L. Skidmore, J. S. Greenbaum, C. Grima, D. A. Young, Discovery of a hypersaline subglacial lake complex beneath Devon Ice Cap, Canadian Arctic. *Science advances*, **4**(4), eaar4353 (2018).

Saarenketo T., Electrical properties of water in clay and silty soils. *Journal of applied geophysics*, **40**(1-3), 73-88 (1998).

Saltas V., F. Vallianatos, D. Triantis, Dielectric properties of non-swelling bentonite: The effect of temperature and water saturation. *Journal of Non-Crystalline Solids*, **354**(52-54), 5533-5541(2008).

Siegert M. J., A 60-year international history of Antarctic subglacial lake exploration. *J. Geol. Soc*. *Lond*. Mem. **461**, 7–21 (2018).

Sihvola A. H., Electromagnetic mixing formulas and applications (No. 47). Iet. (1999).

Smith I. B., D. Lalich, C. Rezza, B. Horgan, J. L. Whitten, S. Nerozzi, J. W. Holt, A Solid Interpretation of Bright Radar Reflectors Under the Mars South Polar Ice. *Geophysical Research Letters*, e2021GL093618 (2021).

Sori M. M., A. M. Bramson, Water on Mars, with a grain of salt: local heat anomalies are required for basal melting of ice at the south pole today. *Geophy. Res. Lett.* **46**(3), 1222-1231 (2019).

Sposito G., R. Prost, Structure of water adsorbed on smectites. *Chemical Reviews*, **82**(6), 553-573 (1982).

Stewart R. D., R. R. Unterberger, Seeing through rock salt with radar. *Geophysics*, **41**(1), 123-132, (1976).

Stillman D. E., J. A. MacGregor, R. E. Grimm, Electrical response of ammonium-rich water ice. *Ann. Glaciol*. **54**(64), 21–26 (2013).

Stillman D. E., R. E. Grimm, Radar penetrates only the youngest geological units on Mars. *J. Geophys. Res. Plan.* **116**(E3) (2011a).

Stillman D. E., R. E. Grimm, S. F. Dec, Low-Frequency Electrical Properties of Ice− Silicate Mixtures. *J. Phys. Chem. B* **114**(18), 6065-6073 (2010).

Stillman D. E., R. E. Grimm. Dielectric signatures of adsorbed and salty liquid water at the Phoenix landing site, Mars. *J. Geophys. Res. Plan.* **116**(E9) (2011b)

Stillman D., G. Olhoeft, Frequency and temperature dependence in electromagnetic properties of Martian analog minerals. *Journal of Geophysical Research: Planets*, **113**(E9), (2008).

Stillman, D. E., Pettinelli, E., Primm, K. M., Caprarelli, G., Mattei, E., Lauro, S. E., & Cosciotti, B. Perchlorate and Chloride Brines as the Cause of the MARSIS Bright Basal Reflections: Laboratory Measurements. *LPI Contributions*, 2614, 6028, (2021).

Tangari A. C., L. Marinangeli, F. Scarciglia, L. Pompilio, E. Piluso, Volcanic holocrystalline bedrock and hydrothermal alteration: a terrestrial analogue for Mars. *Minerals*, **10**(12), 1082 (2020).

Thomas N. H., B. L. Ehlmann, W. Rapin, F. Rivera-Hernández, N. T. Stein, J. Frydenvang, R. C. Wiens, Hydrogen Variability in the Murray Formation, Gale Crater, Mars. Journal of *Geophysical Research: Planets*, **125**(9), e2019JE006289 (2020).

Toner J. D., D. C. Catling, Chlorate brines on Mars: implications for the occurrence of liquid water and deliquescence. *Earth Planet. Sci. Lett.* **497**, 161–168 (2018).

Toner J.D., D.C. Catling, B. Light, The formation of supercooled brines, viscous liquids, and low-temperature perchlorate glasses in aqueous solutions relevant to Mars. *Icarus* **233**, 36-47 (2014).

Treiman A. H., D. L. Bish, D. T. Vaniman, S. J. Chipera, D. F. Blake, D. W. Ming, R. V. Morris, T. F. Bristow, S. M. Morrison, M. B. Baker, E. B. Rampe, R. T. Downs, J. Filiberto, A. F. Glazner, R. Gellert, L. M. Thompson, M. E. Schmidt, L. Le Deit, R. C. Wiens, A. C. McAdam, C. N. Achilles, K. S. Edgett, J. D. Farmer, K. V. Fendrich, J. P. Grotzinger, S. Gupta, J. M. Morookian, M. E. Newcombe, M. S. Rice, J. G. Spray, E. M. Stolper, D. Y. Sumner, A. R. Vasavada, A. S. Yen, Mineralogy, provenance, and diagenesis of a potassic basaltic sandstone on Mars: CheMin X-ray diffraction of the Windjana sample (Kimberley area, Gale crater). *J. Geophys. Res. Planets* **121** ,75–106 (2016).

Treiman A.H., R.A. Barrett, J.L., Gooding, Preterrestrial aqueous alteration of the Lafayette (SNC) meteorite. *Meteoritics* **28**(1), 86-97(1993).

Tulaczyk S. M., N. T. Foley, The role of electrical conductivity in radar wave reflection from glacier beds. *The Cryosphere*, **14**(12), 4495-4506 (2020).

Weir W. B., Automatic measurement of complex dielectric constant and permeability at microwave frequencies. *Proc. IEEE* **62**-1, 33–36 (1974).

828     Wersin P., E. Curti, C. A. J. Appelo, Modelling bentonite–water interactions at high solid/liquid

829     ratios: swelling and diffuse double layer effects. *Applied Clay Science*, **26**(1-4), 249-257 (2004).

830     Wieczorek M.A., Constraints on the composition of the martian south polar cap from gravity

831     and topography. *Icarus* **196**, 506-517 (2008).

832     Young K. F., H. P. R. Frederikse, Compilation of the static dielectric constant of inorganic solids.

833     *Journal of Physical and Chemical Reference Data*, **2**(2), 313-410 (1973).

834

840